



Interplay of structural chemistry and magnetism in perovskites; A study of $\text{CaLn}_2\text{Ni}_2\text{WO}_9$; $\text{Ln}=\text{La}, \text{Pr}, \text{Nd}$

Chun-Mann Chin^a, Robert Paria Sena^b, Emily C. Hunter^a, Joke Hadermann^b, Peter D. Battle^{a,*}

^a Inorganic Chemistry Laboratory, University of Oxford, South Parks Road, Oxford OX1 3QR, UK

^b EMAT, University of Antwerp, Groenenborgerlaan 171, 2020 Antwerp, Belgium

ARTICLE INFO

Keywords:

Perovskite
Magnetism
Diffraction

ABSTRACT

Polycrystalline samples of $\text{CaLn}_2\text{Ni}_2\text{WO}_9$ ($\text{Ln}=\text{La}, \text{Pr}, \text{Nd}$) have been synthesized and characterised by a combination of X-ray and neutron diffraction, electron microscopy and magnetometry. Each composition adopts a perovskite-like structure with $a\sim 5.50$, $b\sim 5.56$, $c\sim 7.78$ Å, $\beta\sim 90.1^\circ$ in space group $P2_1/n$. Of the two crystallographically distinct six-coordinate sites, one is occupied entirely ($\text{Ln}=\text{Pr}$) or predominantly ($\text{Ln}=\text{La}, \text{Nd}$) by Ni^{2+} and the other by Ni^{2+} and W^{6+} in a ratio of approximately 1:2. None of the compounds shows long-range magnetic order at 5 K. The magnetometry data show that the magnetic moments of the Ni^{2+} cations form a spin glass below ~ 30 K in each case. The Pr^{3+} moments in $\text{CaPr}_2\text{Ni}_2\text{WO}_9$ also freeze but the Nd^{3+} moments in $\text{CaNd}_2\text{Ni}_2\text{WO}_9$ do not. This behaviour is contrasted with that observed in other $(A,A')B_2B'\text{O}_9$ perovskites.

1. Introduction

Perovskites, seemingly ubiquitous in solid-state oxide chemistry, have the general formula ABO_3 with at least two distinct cation sites, A and B, in their unit cell. In a simple-cubic perovskite these sites are coordinated by twelve anions at the vertices of a cuboctahedron and six anions at the vertices of an octahedron, respectively. As the ratio of the ionic radii, r_A/r_B , decreases the octahedra tilt, lowering both the symmetry of the structure and the effective coordination number of the A site. The B site can be occupied by a wide variety of cations from either the d block or the f block of the periodic table and in many compounds more than one such cation is present. If they differ significantly in size and charge, they will enter the octahedral sites in an ordered manner and the symmetry of the structure will again be modified. It is also common for more than one species of cation, in this case from Group 2 or the f -block, to occupy the A sites but they are usually distributed in a random fashion rather than in an ordered arrangement. This chemical flexibility has facilitated the synthesis of many compounds with the general formula $(A,A')_2BB'\text{O}_6$ [1] in which two crystallographically-distinct octahedral sites with equal multiplicities are occupied by an ordered, 1:1 alternating arrangement of the cations B and B' . Other ordering schemes have been adopted in perovskites with a $B:B'$ ratio that differs from unity, for example $(A,A')_4B_3B'\text{O}_{12}$ [2] and $(A,A')_3B_2B'\text{O}_9$ [3] where the ordering schemes adopted have two distinct octahedral sites with multiplicity ratios of 3:1 and 2:1, respectively. However, there are a number of $(A,$

$A')_3B_2B'\text{O}_9$ compositions that adopt the 1:1 ordered structure [4,5] even though it is incompatible with the $B:B'$ cation ratio. In these cases, one of the two sites is predominantly occupied by B and the other by a 1:2 ratio of B and B' .

The strongest magnetic interaction in a perovskite is usually the antiferromagnetic coupling that occurs between nearest-neighbour sites along a $\text{B}-\text{O}-\text{B}$ pathway, provided that both the octahedral sites are occupied by a magnetic cation. In a cubic perovskite this pathway is ~ 3.9 Å in length and linear. This leads to an interesting possibility in $(A,A')_3B_2B'\text{O}_9$ compositions that adopt the 1:1 ordered structure with only B being magnetic. In this case antiferromagnetic coupling is expected to lead to a ferrimagnetic material because the different concentration of magnetic cations on the two sublattices with anti-parallel magnetic moments should lead to a non-zero resultant magnetisation. This is exemplified by the behaviour of $\text{Sr}_2\text{LaCr}_2\text{SbO}_9$ [6] which shows long-range ferrimagnetism below ~ 150 K. However, not all $(A,A')_3B_2B'\text{O}_9$ compositions show such ideal behaviour. The spin glass $\text{Sr}_3\text{Fe}_2\text{TeO}_9$ was originally assigned to this structure type [7,8] but has recently been shown [9] to consist of intergrowths of 1:1 and 2:1 ordered structures. The B sites in $\text{SrLa}_2\text{Ni}_2\text{TeO}_9$ both accommodate a mixture of Ni^{2+} and Te^{6+} and the heavily-twinned material appears to contain both spin-glass regions and antiferromagnetic regions [5]. The behaviour of $\text{La}_3\text{Ni}_2\text{SbO}_9$ is different again [4,10]. Neutron diffraction showed that one of the B sites is occupied only by Ni^{2+} and that the other contains a 1:2 mixture of Ni^{2+} and Sb^{5+} . A strong magnetisation was observed below 105 K, suggesting that the behaviour of this

* Corresponding author.

E-mail address: peter.battle@chem.ox.ac.uk (P.D. Battle).

<http://dx.doi.org/10.1016/j.jssc.2017.04.023>

Received 29 March 2017; Received in revised form 19 April 2017; Accepted 20 April 2017

Available online 22 April 2017

0022-4596/ © 2017 The Authors. Published by Elsevier Inc. This is an open access article under the CC BY license (<http://creativecommons.org/licenses/by/4.0/>).

material might be similar to that of $\text{Sr}_2\text{LaCr}_2\text{SbO}_9$. However, only very weak magnetic Bragg scattering was seen in the neutron diffraction pattern recorded at low temperature and, by analogy with the well-known relaxor ferroelectric materials [11,12], it was proposed that $\text{La}_3\text{Ni}_2\text{SbO}_9$ behaves as a relaxor ferromagnet. Evidence for the presence of the necessary domain walls was provided by electron microscopy.

The wide variation in the properties of these $(A,A')_3B_2B'O_9$ phases might be caused by a number of factors including the electron configurations of both the magnetic cation and the non-magnetic cation, the degree of cation ordering on the B sites, the details of the crystal structure and the relative size of the A-site cations. As part of an attempt to elucidate the relative importance of these factors and the extent to which they are interlinked, we have now synthesized and studied $\text{CaLn}_2\text{Ni}_2\text{WO}_9$ for $\text{Ln}=\text{La}$, Pr, Nd. These compositions contain diamagnetic B-site cations with a d^0 electron configuration whereas those studied previously contained d^{10} cations. Furthermore, the presence of Pr^{3+} or Nd^{3+} introduces the possibility of magnetic coupling between the A site and the B sites and the variation in ionic radius with Ln also varies the degree of tilting shown by the octahedra.

2. Experimental

Polycrystalline samples of $\text{CaLn}_2\text{Ni}_2\text{WO}_9$ ($\text{Ln}=\text{La}$, Nd or Pr) were prepared using the traditional ceramic method. In the case of $\text{Ln}=\text{La}$, stoichiometric amounts of NiO , CaCO_3 , WO_3 and pre-dried La_2O_3 were mixed and ground in an agate mortar and pestle before being heated in air at 800 °C for 24 h and at 1150 °C for 6 days. For the syntheses of $\text{CaNd}_2\text{Ni}_2\text{WO}_9$ and $\text{CaPr}_2\text{Ni}_2\text{WO}_9$, La_2O_3 was replaced by Nd_2O_3 and Pr_6O_{11} , respectively, and the high-temperature firing sequence was 1150 °C for 5 days, 1250 °C for 8 days and 1300 °C for 5 days. The reactants were pelletized for all heat treatments above 800 °C and the pellets were ground and reformed every 48–72 h. The reactions were deemed to be complete when the X-ray powder diffraction (XRPD) pattern of the product did not change between successive heatings.

XRPD patterns of the reaction products were collected using a PANalytical Empyrean diffractometer operating with $\text{Cu K}\alpha_1$ radiation ($\lambda=1.54051$ Å) at room temperature. The angular range covered was $5 \leq 2\theta/^\circ \leq 125$ with step-size ($\Delta 2\theta$) of 0.00657°. Neutron powder diffraction (NPD) patterns were collected at various temperatures using the time-of-flight diffractometer GEM at ISIS, United Kingdom [13]. Data from the detector banks located at $2\theta=34.96$ (bank 3), 63.62 (bank 4), 91.30 (bank 5) and 154.40° (bank 6) were analysed using the Rietveld method [14] as implemented in the GSAS program suite [15]. The background level and peak shapes were modelled by a 12-term shifted Chebyshev function and a pseudo-Voigt function, respectively.

A Quantum Design MPMS XL SQUID magnetometer was used to characterise the magnetic properties of $\text{CaLn}_2\text{Ni}_2\text{WO}_9$. Magnetic susceptibility measurements were made in a field of 100 Oe as the sample was warmed through the temperature range $2 \leq T/\text{K} \leq 300$. Measurements were made after the sample had been cooled in the absence of a field (ZFC) and after it had been cooled in the measuring field (FC). For each sample, the field-dependence of the magnetisation per formula unit (f.u.) was measured over the range $-50 \leq H/\text{kOe} \leq 50$ at temperatures that were selected after consideration of the temperature dependence of the magnetic susceptibility.

$\text{CaLa}_2\text{Ni}_2\text{WO}_9$ was also studied by electron microscopy. Specimens were prepared by dispersing crushed powder in ethanol and depositing a few drops of this solution on a copper grid covered with a holey carbon film. SAED patterns were taken with a Philips CM20 transmission electron microscope. High angle annular dark field stem (HAADF-STEM) images and energy dispersive X-ray (EDX) maps were acquired

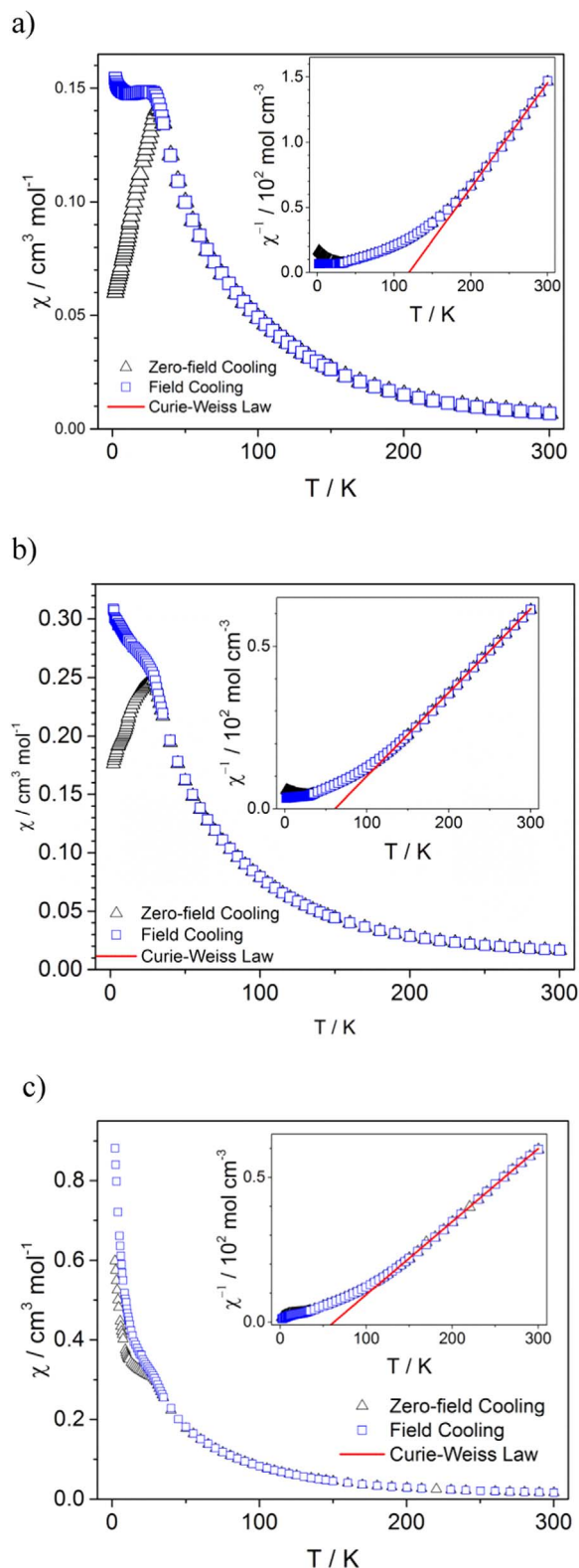


Fig. 1. (a) Temperature dependence of the molar susceptibility and (inset) inverse susceptibility of (a) $\text{CaLa}_2\text{Ni}_2\text{WO}_9$, (b) $\text{CaPr}_2\text{Ni}_2\text{WO}_9$ and (c) $\text{CaNd}_2\text{Ni}_2\text{WO}_9$.

with a FEI Titan 80-300 “cubed” microscope equipped with a Super-X detector and operated at 300 kV.

Table 1
Magnetic parameters of $\text{CaLn}_2\text{Ni}_2\text{WO}_9$ ($\text{Ln}=\text{La}/\text{Pr}/\text{Nd}$).

Composition	C_m	$\mu_{\text{eff}} (\text{Ni})/\mu_B$	θ / K	M_R/μ_B	H_C/kOe	T_g/K
$\text{CaLa}_2\text{Ni}_2\text{WO}_9$	0.805(9)	2.23(2)	+119(3)	0.04	1.5	32
$\text{CaPr}_2\text{Ni}_2\text{WO}_9$	0.250(2)	1.66(1)	+61(2)	0.036	0.75	29
$\text{CaNd}_2\text{Ni}_2\text{WO}_9$	0.257(2)	1.71(1)	+63(2)	0.05	0.4	30

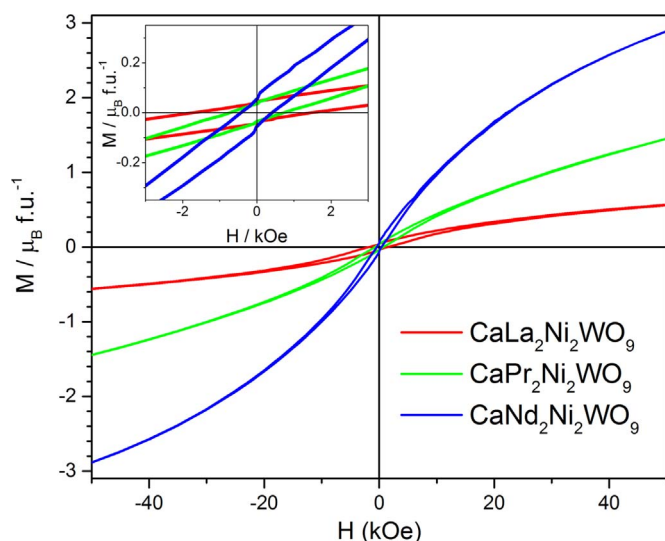


Fig. 2. Field dependence of the magnetisation per formula unit of $\text{CaLa}_2\text{Ni}_2\text{WO}_9$ (red), $\text{CaPr}_2\text{Ni}_2\text{WO}_9$ (green) and $\text{CaNd}_2\text{Ni}_2\text{WO}_9$ (blue) at 5 K. The inset shows the function for $-3 < H/\text{kOe} < 3$. (For interpretation of the references to color in this figure legend, the reader is referred to the web version of this article.)

3. Results

All the final reaction products were dark green in colour. Our preliminary XRPD analysis showed that they all contained a monoclinic, perovskite-like phase and a small trace of unreacted NiO (at most 0.2(4) wt%). In each case the scattering from the principal phase could be accounted for in the space group $P2_1/n$ with $a \sim b \sim \sqrt{2}a_p$, $c \sim 2a_p$ and $\beta \sim 90^\circ$, where a_p is the cell parameter of a primitive cubic perovskite. Rietveld analysis showed that partial ordering of the Ni^{2+} and W^{6+} cations over the two crystallographically-distinct octahedral sites associated with this model is present for all Ln . In contrast, there was no evidence to suggest the presence of ordering among the calcium and lanthanide cations that occupy the A site. Neutron diffraction allows a more precise determination of the atomic coordinates of an oxide perovskite than can be achieved using XRPD and we shall present below a full account of the structure as derived from NPD data.

Fig. 1 shows the temperature dependence of the dc molar magnetic susceptibility of each composition. In the case of $\text{CaLa}_2\text{Ni}_2\text{WO}_9$ the FC susceptibility is essentially constant below 32 K, the temperature at which the ZFC susceptibility reaches a maximum; the two curves overlap above 32 K. The ZFC susceptibility of $\text{CaPr}_2\text{Ni}_2\text{WO}_9$ reaches a maximum at 29 K but the FC susceptibility has a negative temperature gradient throughout the measured range. No maximum is observed in either the ZFC or FC susceptibility of $\text{CaNd}_2\text{Ni}_2\text{WO}_9$, although they take different values below 30 K. The temperature dependence of the inverse susceptibility of each composition is also included in Fig. 1. The data collected in the temperature range $200 \leq T/\text{K} \leq 300$ were fitted to the Curie-Weiss Law; the resulting values of the molar Curie constant,

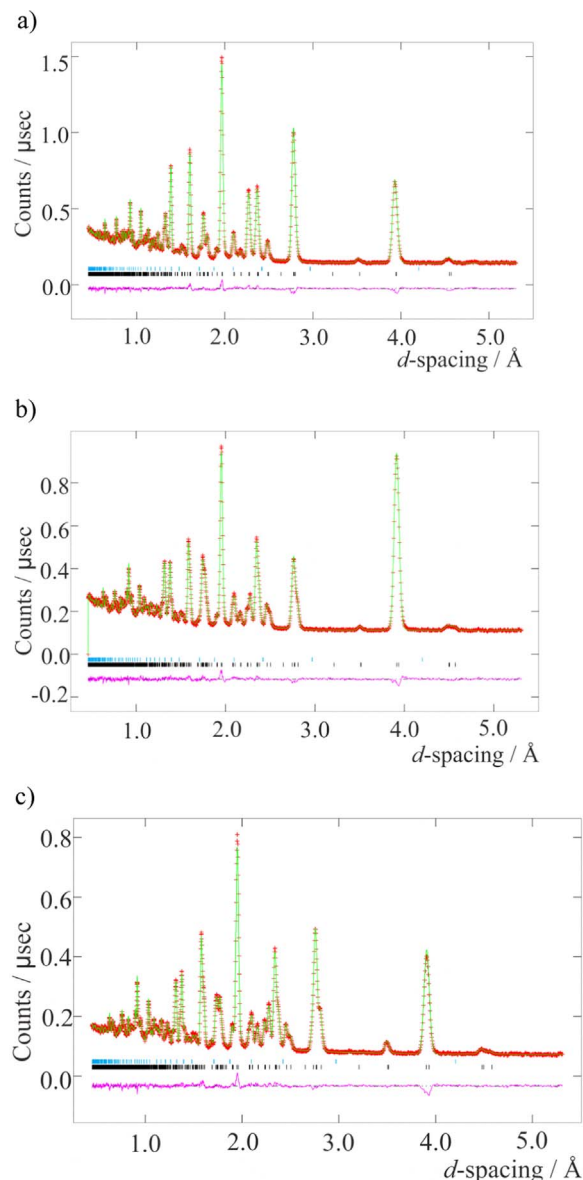


Fig. 3. Observed (red crosses) and calculated (green line) NPD profiles for (a) $\text{CaLa}_2\text{Ni}_2\text{WO}_9$, (b) $\text{CaPr}_2\text{Ni}_2\text{WO}_9$ and (c) $\text{CaNd}_2\text{Ni}_2\text{WO}_9$ at room temperature. A difference curve (purple) is shown below. Reflection positions are marked for NiO (cyan) and the principal phase (black). (For interpretation of the references to color in this figure legend, the reader is referred to the web version of this article.)

C_m , and the Weiss temperature, θ , are listed in Table 1. The value of the effective magnetic moment, μ_{eff} , for the Ni^{2+} cations in each sample is also tabulated. This value was calculated by assuming that the contribution of the Ln^{3+} cations to the Curie constant can be calculated using the Landé formula (Pr^{3+} : $\mu_{\text{eff}}=3.58 \mu_B$; Nd^{3+} : $\mu_{\text{eff}}=3.62 \mu_B$). It was also assumed that the concentration of the NiO impurity was too small to have a significant effect on the bulk magnetic behaviour of the samples. At 5 K, hysteresis is present in $M(H)$ for all three compositions, see Fig. 2, and the magnetisation per formula unit increases from $\text{CaLa}_2\text{Ni}_2\text{WO}_9$ to $\text{CaNd}_2\text{Ni}_2\text{WO}_9$. The remanent magnetisation, M_R , and the coercive field, H_C , as well as the transition temperature, T_g , of $\text{CaLn}_2\text{Ni}_2\text{WO}_9$ are included in Table 1. The field dependence of the magnetisation of each compound at selected temperatures is illustrated more fully in Fig. S1. In each case $M(H)$ was found to be a linear

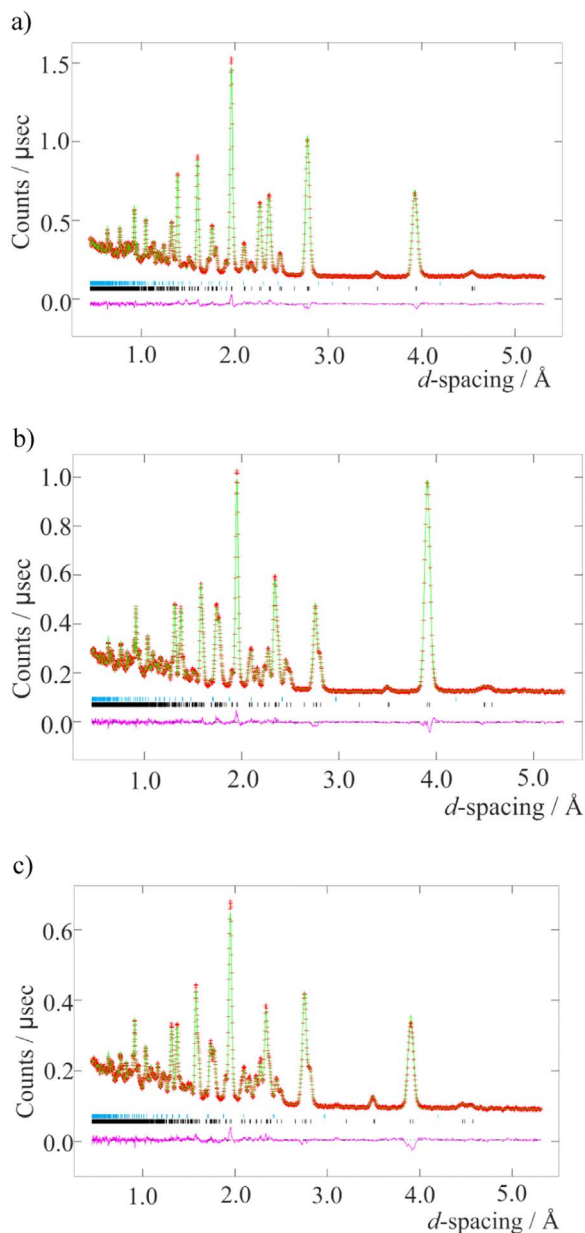


Fig. 4. Observed (red crosses) and calculated (green line) NPD profiles for (a) $\text{CaLa}_2\text{Ni}_2\text{WO}_9$, (b) $\text{CaPr}_2\text{Ni}_2\text{WO}_9$ and (c) $\text{CaNd}_2\text{Ni}_2\text{WO}_9$ at 5 K. A difference curve (purple) is shown below. Reflection positions are marked for NiO (cyan) and the principal phase (black). (For interpretation of the references to color in this figure legend, the reader is referred to the web version of this article.)

function above 150 K.

Rietveld analysis of the neutron diffraction data collected at room temperature using GEM confirmed that the monoclinic $P2_1/n$ structure deduced from XRPD analysis provides a good description of all three solids; no more than ~0.40(1) wt% of unreacted NiO was found in any sample. The fitted patterns recorded using bank 3 at room temperature and 5 K are presented in Figs. 3 and 4. Those recorded on banks 4–6 are shown in Figs. S2–S7. The structural parameters and selected bond distances and bond angles derived from these data are listed in Tables 2–6. The Ni:W ratio was constrained to be 2:1 in all our refinements although the distribution of the cations over the two crystallographically-distinct six-coordinate sites was allowed to vary during the preliminary analysis of the data collected at room temperature. Both cations were found to be present on both sites in $\text{CaLa}_2\text{Ni}_2\text{WO}_9$ and

Table 2

Structural parameters of $\text{CaLa}_2\text{Ni}_2\text{WO}_9$ at room temperature and 5 K (space group $P2_1/n$).

		Room temperature	5 K
$a/\text{\AA}$		5.5320(4)	5.5231(9)
$b/\text{\AA}$		5.5697(4)	5.5671(9)
$c/\text{\AA}$		7.8379(6)	7.8269(12)
$\beta/^\circ$		90.01(1)	89.98(1)
$R_{\text{wp}}/\%$		2.67	3.20
$R_p/\%$		2.57	2.73
χ^2		3.218	4.634
Ca/La	x	0.4887(3)	0.4870(3)
4e ($x y z$)	y	0.4635(2)	0.4619(2)
	z	0.2506(7)	0.2511(8)
	$U_{\text{iso}}/\text{\AA}^2$	0.0188(2)	0.0146(2)
	Ca occupancy	0.3333	0.3333
	La occupancy	0.6667	0.6667
Ni/W1	$U_{\text{iso}}/\text{\AA}^2$	0.0037(3)	0.0025(3)
2c ($0 \frac{1}{2} 0$)	Ni occupancy	0.965(5)	0.965
	W occupancy	0.035(5)	0.035
Ni/W2	$U_{\text{iso}}/\text{\AA}^2$	0.0042(4)	0.0015(4)
2d ($\frac{1}{2} 0 0$)	Ni occupancy	0.368(5)	0.368
	W occupancy	0.632(5)	0.632
O1	x	0.7835(6)	0.7819(6)
4e ($x y z$)	y	0.7913(7)	0.7934(8)
	z	−0.0438(4)	−0.0352(4)
	$U_{\text{iso}}/\text{\AA}^2$	0.0103(8)	0.0078(7)
O2	x	0.7033(6)	0.7004(6)
4e ($x y z$)	y	0.2868(7)	0.2869(8)
	z	−0.0326(4)	−0.0426(4)
	$U_{\text{iso}}/\text{\AA}^2$	0.0082(8)	0.0059(7)
O3	x	0.5777(3)	0.5780(3)
4e ($x y z$)	y	0.0157(2)	0.0159(2)
	z	0.2435(7)	0.2448(9)
	$U_{\text{iso}}/\text{\AA}^2$	0.0095(4)	0.0061(4)

Table 3

Structural parameters of $\text{CaPr}_2\text{Ni}_2\text{WO}_9$ at room temperature and 5 K (space group $P2_1/n$).

		Room temperature	5 K
$a/\text{\AA}$		5.4681(3)	5.4537(3)
$b/\text{\AA}$		5.5989(3)	5.6011(3)
$c/\text{\AA}$		7.7800(4)	7.7651(4)
$\beta/^\circ$		90.142(2)	90.174(2)
$R_{\text{wp}}/\%$		2.46	2.49
$R_p/\%$		2.11	2.12
χ^2		2.251	2.505
Ca/Pr	x	0.4892(3)	0.4888(3)
4e ($x y z$)	y	0.4510(2)	0.4484(1)
	z	0.2521(5)	0.2518(4)
	$U_{\text{iso}}/\text{\AA}^2$	0.0203(2)	0.0155(2)
	Ca occupancy	0.3333	0.3333
	Pr occupancy	0.6667	0.6667
Ni/W1	$U_{\text{iso}}/\text{\AA}^2$	0.0029(2)	0.0013(2)
2c ($0 \frac{1}{2} 0$)	Ni occupancy	1	1
	W occupancy	0	0
Ni/W2	$U_{\text{iso}}/\text{\AA}^2$	0.0036(3)	0.0014(2)
2d ($\frac{1}{2} 0 0$)	Ni occupancy	0.3333	0.3333
	W occupancy	0.6667	0.6667
O1	x	0.7903(3)	0.7904(2)
4e ($x y z$)	y	0.8027(3)	0.8039(3)
	z	−0.0408(2)	−0.0419(2)
	$U_{\text{iso}}/\text{\AA}^2$	0.0077(4)	0.0046(3)
O2	x	0.6945(3)	0.6936(2)
4e ($x y z$)	y	0.2896(3)	0.2884(2)
	z	−0.0463(2)	−0.0467(2)
	$U_{\text{iso}}/\text{\AA}^2$	0.0073(4)	0.0044(3)
O3	x	0.5842(1)	0.5854(1)
4e ($x y z$)	y	0.0235(1)	0.0238(1)
	z	0.2446(2)	0.2441(2)
	$U_{\text{iso}}/\text{\AA}^2$	0.0074(2)	0.0043(2)

Table 4Structural parameters of $\text{CaNd}_2\text{Ni}_2\text{WO}_9$ at room temperature and 5 K (space group $P2_1/n$).

		Room temperature	5 K
$a/\text{\AA}$		5.4441(6)	5.4304(8)
$b/\text{\AA}$		5.6097(6)	5.6131(8)
$c/\text{\AA}$		7.7597(9)	7.7461(11)
$\beta/^\circ$		90.184(2)	90.229(2)
$R_{\text{wp}}/\%$		2.66	2.92
$R_p/\%$		2.91	2.87
χ^2		2.253	2.630
Ca/Nd	x	0.4880(2)	0.4882(2)
4e ($x\ y\ z$)	y	0.4466(1)	0.4446(1)
	z	0.2530(4)	0.2530(4)
	$U_{\text{iso}}/\text{\AA}^2$	0.0162(2)	0.0113(2)
	Ca occupancy	0.3333	0.3333
Ni/W1	Nd occupancy	0.6667	0.6667
	$U_{\text{iso}}/\text{\AA}^2$	0.0031(1)	0.0007(3)
	Ni occupancy	0.971(6)	0.971
	W occupancy	0.029(6)	0.029
Ni/W2	$U_{\text{iso}}/\text{\AA}^2$	0.0043(5)	0.0012(4)
	Ni occupancy	0.362(6)	0.362
	W occupancy	0.638(6)	0.638
	x	0.7922(3)	0.7922(3)
2c ($0\ \frac{1}{2}\ 0$)	y	0.8046(3)	0.8056(3)
	z	−0.0424(2)	−0.0432(2)
	$U_{\text{iso}}/\text{\AA}^2$	0.0071(4)	0.0035(3)
	x	0.6924(3)	0.6907(3)
O1	y	0.2903(3)	0.2903(3)
	z	−0.0481(3)	−0.0484(2)
	$U_{\text{iso}}/\text{\AA}^2$	0.0074(4)	0.0028(3)
	x	0.5874(2)	0.5878(2)
O2	y	0.0253(2)	0.0256(2)
	z	0.2445(3)	0.2437(3)
	$U_{\text{iso}}/\text{\AA}^2$	0.0070(2)	0.0027(2)
	x		
O3	y		
	z		
	$U_{\text{iso}}/\text{\AA}^2$		

$\text{CaNd}_2\text{Ni}_2\text{WO}_9$ but in $\text{CaPr}_2\text{Ni}_2\text{WO}_9$ the 2c site was found to be occupied only by Ni^{2+} ; a constraint imposing this condition was employed in our final refinements. The Ni/W distributions deduced from the data collected at room temperature were held fixed during the analyses of the NPD datasets collected at 5 K. No magnetic Bragg scattering was observable at large d -spacings in any of latter datasets. In the case of $\text{CaPr}_2\text{Ni}_2\text{WO}_9$, an additional data set was collected at 20 K; the fitted pattern and the corresponding structural parameters are presented in Fig. S8 and Table S1.

Selected area electron diffraction (SAED) patterns, including several tilt series, were taken from many different crystals of $\text{CaLa}_2\text{Ni}_2\text{WO}_9$. All the patterns could be indexed using the cell parameters obtained from Rietveld analysis of the XRPD data. Fig. 5 shows representative SAED patterns from the main zone axes ($[001,010,100]$ and $[110]$). They are in agreement with the reflection conditions for $P2_1/n$: $[010]$ shows clearly that $h0l$: $h+l=2n$, $h00$: $h=2n$ and $00l$: $l=2n$. The presence on some of the other patterns of $h00$: $h=2n+1$ and $00l$: $l=2n+1$ reflections, which should be absent in $P2_1/n$, is attributable to double diffraction. The presence of the $0k0$: $k=2n+1$ reflections is also due to double diffraction, as was verified by tilting around the b^* -axis until these reflections disappeared. We note that calculated electron diffraction patterns along $[010]$ and $[111]$ are indistinguishable for this structure in space group $P2_1/n$ (in the parent perovskite they are symmetry equivalent $\langle 110 \rangle_p$). It is thus possible to index $[111]$ incorrectly as $[010]$. However no other patterns corresponding to $\langle 110 \rangle_p$ were found in the sample except the two labelled as $[100]$ and $[010]$ in Fig. 5. Fig. 6 shows high resolution

HAADF-STEM images taken along two main zones. On both the $[100]$ and the $[010]$ image a clear alternation in brightness is seen in the rows containing the B cations, i.e. the alternation between columns containing W and no W (W has atomic number $Z=74$ and thus gives the very bright dots on the image). This is in agreement with the chess board order of the B cations found in the $P2_1/n$ model. Fig. 7 shows the composition of each column viewed along $[010]$ as obtained by high resolution STEM-EDX imaging. Ca and La are seen to be disordered. However, W occupies just one of the two B columns along this projection whereas Ni occupies both, but with a higher concentration in the W – free column; oxygen cannot be reliably mapped due to its low atomic number.

4. Discussion

As is to be expected, the unit cell parameters of $\text{CaLn}_2\text{Ni}_2\text{WO}_9$ decrease at both room temperature and 5 K as the atomic number of Ln increases. In each composition the distortion away from the cubic symmetry of an ideal perovskite reduces the coordination number of the Ca/Ln site from twelve to eight, see Tables 5 and 6. There is a significant decrease in the mean $\text{Ca}/Ln\text{--O}$ bond length between $\text{CaLa}_2\text{Ni}_2\text{WO}_9$ and $\text{CaPr}_2\text{Ni}_2\text{WO}_9$ but the change is less marked when Pr^{3+} is replaced by Nd^{3+} . The Ni/W–O bond lengths around the Ni-rich 2c site are always longer than those around the W-rich 2d site. For $Ln=\text{Pr}$ or Nd the octahedron surrounding the site dominated by the hexavalent cation contains two very similar, relatively short 2d–O distances and one longer distance, as was the case in $\text{SrLa}_2\text{Ni}_2\text{TeO}_9$; two relatively long bond lengths and one shorter distance are found around the 2c site. However, this pseudo-tetragonal environment is not apparent in the less-precise bond lengths tabulated for $Ln=\text{La}$. The 2c–O–2d bond angles, which play an important role in determining the strength of the magnetic superexchange interactions, deviate further from 180° as the ionic radius of Ln decreases. The degree of Ni/W ordering varies between the three compounds in a manner that does not correlate with the unit cell volume and it is not clear what factors do cause the variation. However, the degree of ordering is always higher than was observed in $\text{SrLa}_2\text{Ni}_2\text{TeO}_9$ [5]. Our study of $\text{CaLa}_2\text{Ni}_2\text{WO}_9$ by electron microscopy did not reveal any anomalies in the microstructure of the compound. The HAADF-STEM and EDX images, see Figs. 6 and 7, show that the crystal selected for detailed study had very well-developed cation ordering over the B sites, with W^{6+} only present on one crystallographic site in the chosen region. The apparent occurrence of some $\text{La}^{3+}/\text{Ca}^{2+}$ cations on the six-coordinate sites is an artifact, due to the signal of Ca being very noisy. For clarity, the maps are shown in counts, not atomic percent, which unfortunately also increases the visibility of the noise related to the Ca map.

The values of the effective magnetic moment of Ni^{2+} derived by fitting the temperature dependence of the susceptibility to the Curie-Weiss law, see Table 1, are all significantly below the spin-only value, indicating that significant short-range interactions are present in all three compounds above 220 K. The reduced values of μ_{eff} and the positive values of the Weiss temperature, θ , suggest that the magnetic moments on nearest-neighbour Ni^{2+} cations couple antiferromagnetically and that the imbalance in their numbers leads to the presence of uncoupled ferrimagnetic regions. The behaviour observed at relatively high temperatures thus suggests that these compounds might, like $\text{LaSr}_2\text{Cr}_2\text{SbO}_9$, order as ferrimagnets on cooling.

However, the absence of magnetic Bragg scattering from the neutron diffraction patterns collected at 5 K shows that there is no long-range magnetic order in any of the compounds under consideration at that temperature. We therefore conclude that the behaviours of

Table 5Selected bond lengths (Å) and angles (°) in $\text{CaLn}_2\text{Ni}_2\text{WO}_9$ ($\text{Ln}=\text{La}$, Pr or Nd) at RT.

	$\text{CaLa}_2\text{Ni}_2\text{WO}_9$	$\text{CaPr}_2\text{Ni}_2\text{WO}_9$	$\text{CaNd}_2\text{Ni}_2\text{WO}_9$
Ca/Ln-O1	2.791(6)	2.679(4)	2.663(3)
Ca/Ln-O1	2.628(5)	2.653(3)	2.639(3)
Ca/Ln-O1	2.398(5)	2.385(3)	2.370(3)
Ca/Ln-O2	2.703(6)	2.735(4)	2.735(3)
Ca/Ln-O2	2.445(5)	2.382(3)	2.379(3)
Ca/Ln-O2	2.707(5)	2.624(3)	2.599(3)
Ca/Ln-O3	2.543(1)	2.450(1)	2.425(1)
Ca/Ln-O3	2.417(3)	2.368(2)	2.353(2)
$2c\text{-O1}$	2.046(4)×2	2.070(2)×2	2.075(2)×2
$2c\text{-O2}$	2.042(3)×2	2.075(1)×2	2.079(2)×2
$2c\text{-O3}$	2.057(5)×2	2.045(2)×2	2.046(2)×2
$2d\text{-O1}$	1.982(3)×2	1.960(1)×2	1.960(2)×2
$2d\text{-O2}$	1.970(4)×2	1.973(2)×2	1.973(2)×2
$2d\text{-O3}$	1.959(5)×2	1.961(2)×2	1.959(2)×2
$\text{O1-}2c\text{-O2}$	88.3(2)×2	89.6(1)×2	89.9(1)×2
$\text{O1-}2c\text{-O3}$	89.6(1)×2	88.3(1)×2	88.2(1)×2
$\text{O2-}2c\text{-O3}$	88.8(1)×2	88.7(1)×2	88.7(1)×2
$\text{O1-}2d\text{-O2}$	89.9(2)×2	89.8(1)×2	89.9(1)×2
$\text{O1-}2d\text{-O3}$	88.8(1)×2	89.6(1)×2	89.5(1)×2
$\text{O2-}2d\text{-O3}$	88.0(1)×2	89.8(1)×2	89.8(1)×2
$2c\text{-O1-}2d$	154.1(2)	152.2(1)	151.2(1)
$2c\text{-O2-}2d$	156.1(2)	150.4(1)	149.4(1)
$2c\text{-O3-}2d$	154.8(1)	152.33(4)	151.3(1)

Table 6Selected bond lengths (Å) and angles (°) in $\text{CaLn}_2\text{Ni}_2\text{WO}_9$ ($\text{Ln}=\text{La}$, Pr or Nd) at 5 K.

	$\text{CaLa}_2\text{Ni}_2\text{WO}_9$	$\text{CaPr}_2\text{Ni}_2\text{WO}_9$	$\text{CaNd}_2\text{Ni}_2\text{WO}_9$
Ca/Ln-O1	2.730(6)	2.677(3)	2.657(3)
Ca/Ln-O1	2.661(6)	2.638(3)	2.629(3)
Ca/Ln-O1	2.436(6)	2.382(3)	2.367(3)
Ca/Ln-O2	2.761(7)	2.727(3)	2.726(3)
Ca/Ln-O2	2.386(6)	2.385(3)	2.379(3)
Ca/Ln-O2	2.651(6)	2.610(3)	2.595(3)
Ca/Ln-O3	2.534(2)	2.436(1)	2.415(1)
Ca/Ln-O3	2.422(3)	2.361(2)	2.347(2)
$2c\text{-O1}$	2.048(4)×2	2.076(1)×2	2.080(2)×2
$2c\text{-O2}$	2.064(3)×2	2.080(1)×2	2.084(1)×2
$2c\text{-O3}$	2.045(7)×2	2.047(2)×2	2.049(2)×2
$2d\text{-O1}$	1.955(4)×2	1.956(1)×2	1.956(2)×2
$2d\text{-O2}$	1.971(4)×2	1.964(1)×2	1.968(2)×2
$2d\text{-O3}$	1.966(7)×2	1.955(2)×2	1.951(2)×2
$\text{O1-}2c\text{-O2}$	88.0(2)×2	89.9(1)×2	90.0(1)×2
$\text{O1-}2c\text{-O3}$	88.5(1)×2	88.4(1)×2	88.3(1)×2
$\text{O2-}2c\text{-O3}$	89.2(1)×2	88.8(1)×2	88.7(1)×2
$\text{O1-}2d\text{-O2}$	89.7(2)×2	89.7(1)×2	89.9(1)×2
$\text{O1-}2d\text{-O3}$	89.4(1)×2	89.5(1)×2	89.4(1)×2
$\text{O2-}2d\text{-O3}$	89.7(1)×2	89.8(1)×2	89.8(1)×2
$2c\text{-O1-}2d$	156.7(2)	151.7(1)	150.8(1)
$2c\text{-O2-}2d$	152.7(2)	150.3(1)	149.1(1)
$2c\text{-O3-}2d$	154.7(1)	151.96(4)	151.2(1)

$\chi(T)$ below 50 K, see Fig. 1, and the hysteresis seen in $M(H)$, see Fig. 2, are associated with the formation of spin-glass phases at low temperature. However, the three compounds all behave differently, presumably because of the differing magnetic properties of Ln^{3+} . In the case of $\text{CaLa}_2\text{Ni}_2\text{WO}_9$ the ZFC $\chi(T)$ curve shows a maximum at 32 K and the FC is constant for $T < T_K < 32$. This is canonical behaviour for a spin glass and suggests that the spins of the Ni^{2+} cations freeze at 32 K. However, there is evidence for a change in the FC susceptibility close to the low-temperature limit of our instrument. It would be necessary to perform further experiments at lower temperatures in order to arrive at an explanation for this behaviour. The FC susceptibility of $\text{CaPr}_2\text{Ni}_2\text{WO}_9$ has a maximum at a similar temperature, 29 K, but in this case the FC susceptibility has a negative temperature gradient throughout the measured region. The absence of a paramagnetic component in the ZFC susceptibility below 29 K suggests that the spins of not only the Ni^{2+} cations but also those of the Pr^{3+} cations freeze at the transition temperature. The behaviour of the FC susceptibility below T_g can be ascribed to the presence of entropic clusters [16]. Finally, although there is clearly a transition at 30 K in $\chi(T)$ for $\text{CaNd}_2\text{Ni}_2\text{WO}_9$, both the ZFC and the FC curves show a negative gradient that increases with decreasing temperature down to 2 K. In order to account for this behaviour we propose that the Ni^{2+} spins freeze at 30 K, but those of the Nd^{3+} cations remain paramagnetic throughout the measured temperature range. It is not surprising that the compound containing diamagnetic La^{3+} behaves differently from those containing paramagnetic Pr^{3+} or Nd^{3+} ; it is more surprising that there is such a marked difference between the latter pair [17]. The answer might lie in the anisotropy difference between the two cations.

Finally, we note that when only nearest-neighbour (NN) superexchange is operative the perovskite structure is not frustrated and the formation of a spin-glass phase is not to be expected. The occurrence of such behaviour, seen in many perovskites [18,19], can be ascribed to

frustration caused by competition between NN and next-nearest-neighbour (NNN) superexchange interactions, the relative strengths of which will depend on the $2c\text{-O-}2d$ bond angle and, locally, on variations in the cation distribution. Only one of the $(A,A')B_2B'\text{O}_9$ perovskites that we have studied to date shows simple long-range magnetic ordering. That compound, $\text{LaSr}_2\text{Cr}_2\text{SbO}_9$, has a lower level of cation ordering over the two six-coordinate sites than any of the tungsten-based compounds described above, demonstrating that such ordering is not essential for magnetic ordering. However, the NN superexchange pathway in $\text{LaSr}_2\text{Cr}_2\text{SbO}_9$ is closer to linearity than that in $\text{SrLa}_2\text{Ni}_2\text{TeO}_9$ or any of the compounds studied in this work. It is therefore possible that the $2c\text{-O-}2d$ bond angle plays a key role in determining whether or not these compounds show long-range magnetic order in their ground state.

5. Conclusion

Although the high-temperature susceptibility data indicate the presence of strong short-range magnetic coupling, $\text{CaLn}_2\text{Ni}_2\text{WO}_9$ ($\text{Ln}=\text{La}$, Pr, Nd), unlike $\text{LaSr}_2\text{Cr}_2\text{SbO}_9$, do not show long-range magnetic order at 5 K. Nor do they show a high magnetisation at low temperatures despite the absence of magnetic Bragg scattering, as did the relaxor-ferromagnet $\text{La}_3\text{Ni}_2\text{SbO}_9$. Their behaviour is most similar to that of $\text{SrLa}_2\text{Ni}_2\text{TeO}_9$ which was described as a spin glass with islands of long-range antiferromagnetic order. However, the absence of these islands in the present case means that we have identified yet another type of magnetic behaviour in this rather limited family of compounds. The frustration necessary for spin-glass formation is thought to stem from competition between NN and NNN superexchange interactions, the strength of which correlates with the linearity of the NN superexchange pathway; variations in the local composition might also play a role.

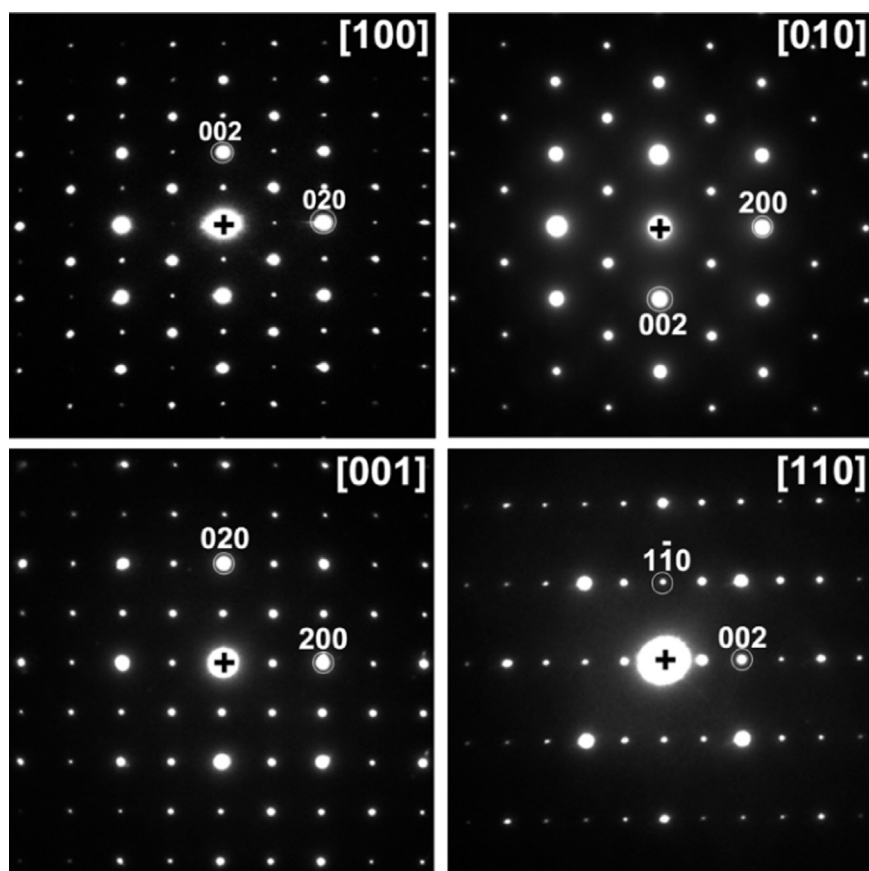


Fig. 5. Representative selected-area electron-diffraction patterns of $\text{CaLa}_2\text{Ni}_2\text{WO}_9$.

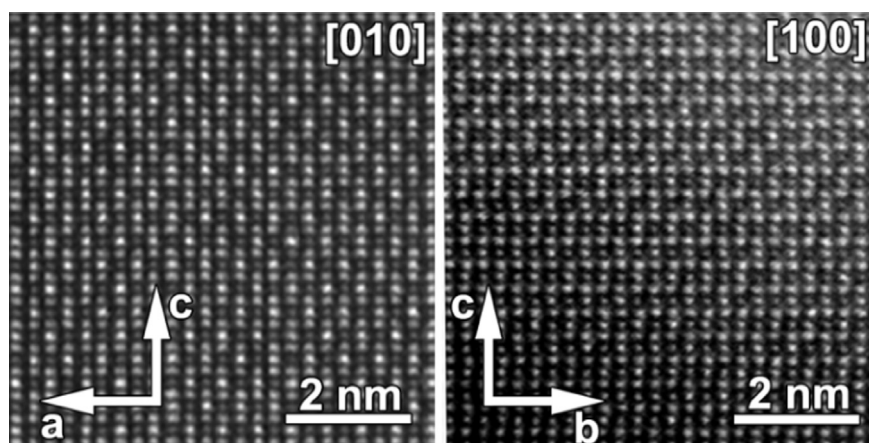


Fig. 6. High-resolution HAADF STEM image along the [100] and [010] zone axes of $\text{CaLa}_2\text{Ni}_2\text{WO}_9$. The images were corrected for drift and a low band pass filter was applied.

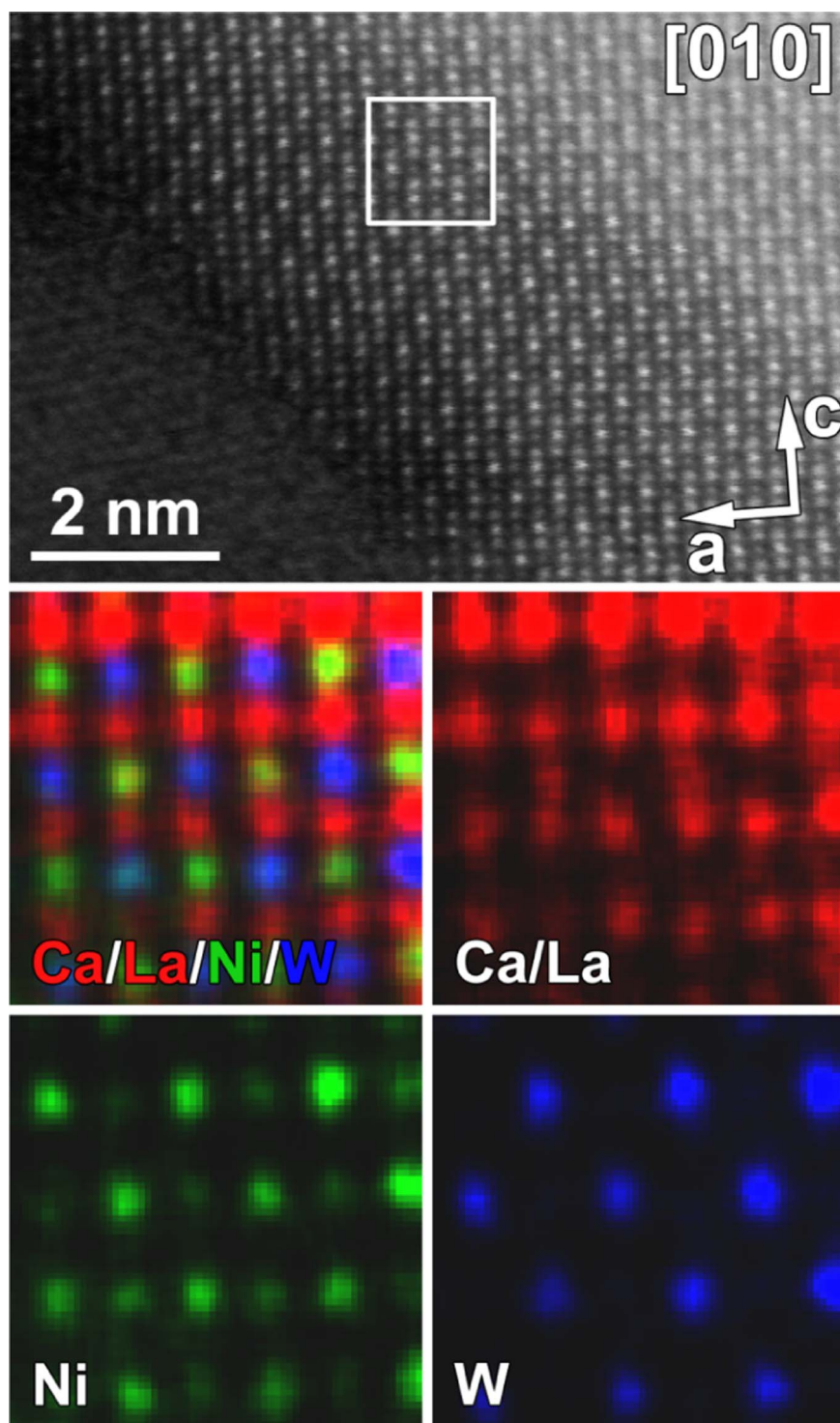


Fig. 7. High resolution EDX map of the [010] zone. The HAADF-STEM image of the surrounding area is shown at the top, the exact area taken for the EDX map shown below is indicated by a white rectangle.

Acknowledgments

We thank EPSRC for funding through grant EP/M0189541. CMC thanks the Croucher Foundation and Oxford University for a graduate scholarship. We are grateful to Ivan da Silva who provided experimental assistance at ISIS and to Maria Batuk for help with the STEM-EDX analysis.

Appendix A. Supplementary material

Supplementary data associated with this article can be found in the online version at [doi:10.1016/j.jssc.2017.04.023](https://doi.org/10.1016/j.jssc.2017.04.023).

References

- [1] M.T. Anderson, K.B. Greenwood, G.A. Taylor, K.R. Poeppelmeier, *Prog. Solid State Chem.* 22 (1993) 197–233.
- [2] A.J. Jacobson, B.M. Collins, B.E.F. Fender, *Acta Crystallogr. B* 30 (1974) 1705.
- [3] U. Treiber, S. Kemmler Sack, *J. Solid State Chem.* 43 (1982) 51–62.
- [4] P.D. Battle, S.I. Evers, E.C. Hunter, M. Westwood, *Inorg. Chem.* 52 (2013) 6648.
- [5] R. Paria Sena, J. Hadermann, C.M. Chin, E.C. Hunter, P.D. Battle, *J. Solid State Chem.* 243 (2016) 304–311.
- [6] E.C. Hunter, P.D. Battle, R. Paria Sena, J. Hadermann, *J. Solid State Chem.* 248 (2017) 96–103.
- [7] M.S. Augsburger, M.C. Viola, J.C. Pedregosa, R.E. Carbonio, J.A. Alonso, *J. Mater. Chem.* 16 (2006) 4235–4242.
- [8] S.A. Ivanov, P. Nordblad, S.G. Eriksson, R. Tellgren, H. Rundlof, *Mater. Res. Bull.* 42 (2007) 776–789.
- [9] Y.W. Tang, E.C. Hunter, P.D. Battle, R. Paria Sena, J. Hadermann, M. Avdeev, J.M. Cadogan, *J. Solid State Chem.* 242 (2016) 86–95.
- [10] P.D. Battle, M. Avdeev, J. Hadermann, *J. Solid State Chem.* 220 (2014) 163.
- [11] A.A. Bokov, Z.G. Ye, *J. Mater. Sci.* 41 (2006) 31–52.
- [12] P.K. Davies, M.A. Akbas, *J. Phys. Chem. Solids* 61 (2000) 159–166.
- [13] W.G. Williams, R.M. Ibberson, P. Day, J.E. Enderby, *Phys. B-Condens. Matter* 241 (1997) 234–236.
- [14] H.M. Rietveld, *J. Appl. Crystallogr.* 2 (1969) 65–71.
- [15] A.C. Larson, R.B. von-Dreele, *General Structure Analysis System (GSAS)*, Los Alamos National Laboratories LAUR 86-748, 1994.
- [16] D. Fiorani, S. Viticoli, J.L. Dormann, J.L. Tholence, A.P. Murani, *Phys. Rev. B* 30 (1984) 2776.
- [17] J. Prado-Gonjal, R. Schmidt, J.J. Romero, D. Avila, U. Amador, E. Moran, *Inorg. Chem.* 52 (2013) 313–320.
- [18] E.J. Cussen, J.F. Vente, P.D. Battle, T. Gibb, *J. Mater. Chem.* 7 (1997) 459.
- [19] R. Rodriguez, A. Fernandez, A. Isalgue, J. Rodriguez, A. Labarta, J. Tejada, X. Obradors, *J. Phys. C: Solid State Phys.* 18 (1985) L401.